

## Solar light degradation of organic dye pollutants and preparation of bis(indolyl) methanes using core-shell $\text{Fe}_3\text{O}_4@ \text{SiO}_2@ \text{CuO}$ nanocomposite

Kaveh PARVANAK BOROUJENI<sup>1\*</sup>, Zeinab TOHIDIYAN<sup>2</sup>, Mina MIRZAEI<sup>1</sup>

<sup>1</sup>Department of Chemistry, Shahrekord University, Shahrekord, Iran

<sup>2</sup>Department of Chemistry, Shahrekord Branch, Islamic Azad University, Shahrekord, Iran

Received: 15.04.2021 • Accepted/Published Online: 10.08.2021 • Final Version: 23.02.2022

**Abstract:** In this research, a new ferromagnetic-recoverable core-shell  $\text{Fe}_3\text{O}_4@ \text{SiO}_2@ \text{CuO}$  nanocomposite of a certain size (20–25 nm) has been synthesized based on Cu(II) complex coated on  $\text{Fe}_3\text{O}_4@ \text{SiO}_2$  nanoparticles by facile and fast solid state microwave irradiation method. The photocatalytic activity of the nanocomposite was investigated for degradation of methylene blue (MB) and methyl orange (MO) dye pollutants in aqueous media under solar light irradiation. The nanocomposite could destroy these dyes with high efficiency in short time. With comparison of degradation percentages can be concluded that the nanocomposite shows better photocatalytic activity for MB dye (97% in 180 s). Kinetic study revealed higher rate constant for degradation of MB ( $k = 3.6 \times 10^{-3} \text{ s}^{-1}$ ) with pseudozero-order model. Also,  $\text{Fe}_3\text{O}_4@ \text{SiO}_2@ \text{CuO}$  nanocomposite was an efficient magnetically recoverable catalyst for the preparation of bis(indolyl) methanes (BIMs) through the condensation of an aldehyde with 2 equivalents of indole in EtOH/ $\text{H}_2\text{O}$  as green solvents.

**Key words:** Core-shell  $\text{Fe}_3\text{O}_4@ \text{SiO}_2@ \text{CuO}$  nanocomposite, microwave irradiation, solar-light photocatalytic degradation, bis(indolyl) methanes, catalysis

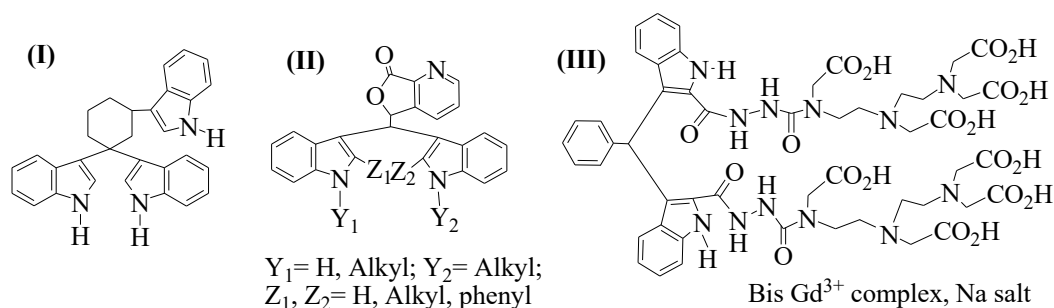
### 1. Introduction

Nowadays, protection of the environment has received considerable attention. Polluter compounds are spread in the environment from various sources. A type of hazardous polluter compounds are organic dyes, generated by industrial processes. The growing amount of different organic dyes in waste water is a worrying issue for human health and live species [1]. Consequently, it is necessary to develop strategies for removing them from environmental systems. Many techniques such as coagulation, flocculation, reverse osmosis, adsorption on the activated carbon, ultrafiltration, and adsorption have been reported as effective ways to remove the toxic dyes from waste water [2,3]. In recent years, photocatalytic degradation reactions have emerged as an alternative approach for the removal of different dye pollutants from waste water [4]. In fact, photocatalytic degradation reactions are oxidation processes which lead to complete degradation of dye pollutants in short times and even at low concentration. Due to versatility and relative simplicity along with high degradation efficiency, much research effort has focused on design and preparation of various photocatalysts [5,6].

Core-shell nanostructures are complex systems that involve the benefits of both core and shell to improve physiochemical properties. The core usually consists of the inexpensive and easily oxidized metals and the shells include somewhat noble metals, metal oxides, available carbon materials, polymers, silica, and so on [7]. Different methods have been explored in the synthesis of core-shell systems, such as hydrothermal, deposition-precipitation, and sonochemical method [8]. Among core-shell nanostructures, core-shell composites with  $\text{Fe}_3\text{O}_4$  at the center have been widely used because of their characteristic properties such as easy separation from reaction vessel via an external magnet and subsequent use in catalytic reactions, chemical stability, nontoxicity, high selectivity and activity performance, and suitable industrial and biomedical applications [9,10]. However, applications of core-shell composites in catalytic field for preparing organic compounds are rare. For instances, dendrimer-encapsulated Cu(II) nanoparticles supported on superparamagnetic  $\text{Fe}_3\text{O}_4@ \text{SiO}_2$  nanoparticles and  $\text{Fe}_3\text{O}_4@ \text{SiO}_2$  nanoparticles have been applied as catalysts for the preparation of 5-substituted 1H-tetrazoles [11] and the synthesis of tetrahydrobenzo[a]xanthen-11-ones [12], respectively.

BIMs are compounds consisting of two indolyl moieties which are connected to each other by a carbon atom [13]. BIMs can be obtained either from different earthly and marine natural sources or by the laboratory methods. The prominent biological activities associated with BIMs are antimicrobial, antifungal, analgesic, and antiinflammatory [14,15]. They are inhibitors of bladder cancer [16]. Anticancer effects of 1,1,3-tri(3-indolyl)cyclohexane (Scheme 1, I) in various lung cancer

\* Correspondence: parvanak-ka@sku.ac.ir



**Scheme 1.** Biological applications of a series of BIM derivatives.

cells were surveyed [17]. Chromogenic 3,3'-bisindolyl-4-azaphthalides (II) [18] has been employed as color formers in pressure-sensitive or heat-sensitive recording materials. Also, complex (III) based on BIMs containing radioactive metal ions (Gd<sup>3+</sup>) [19] has been used as a contrast agent for radio-imaging and visualization of various tissues and organs. One of the most frequently used methods for the preparation of BIMs is the electrophilic substitution reaction of indole with aldehydes and ketones. This reaction is usually catalyzed by several types of catalysts such as InCl<sub>3</sub> [20], LiClO<sub>4</sub> [21], I<sub>2</sub> [22], sulfamic acid [23], HBF<sub>4</sub>-SiO<sub>2</sub> [24], poly(ethylene-glycol)-sulfonic acid (PEG-SO<sub>3</sub>H) [25], sulfonated polyacrylamide [26], SiO<sub>2</sub>-AlCl<sub>3</sub> [27], Nafion-H<sup>®</sup> [28], [DABCO-H][HSO<sub>4</sub>] [29], nano *n*-propylsulfonated  $\gamma$ -Fe<sub>2</sub>O<sub>3</sub> [30], Sc(OTf)<sub>3</sub> [31], CaO [32], graphene oxide [33], 4-(3-methylimidazolium)butane sulfonate (MBS) [34], hyper-cross-linked polyaromatic spheres (HCP@CH<sub>2</sub>Br) [35], itaconic acid [36], borophosphate glasses [37], and BF<sub>3</sub>-grafted Fe<sub>3</sub>O<sub>4</sub>@sucrose nanoparticles [38]. However, many of these reported synthetic protocols suffer from some disadvantages like long reaction time, low yields, strongly acidic conditions, tedious work-up, the use of toxic solvents, formation of by-products, and difficulty of recovery and recycling. Therefore, the preparation of BIMs seems still a challenge, especially from the viewpoint of green chemistry.

Recently, we introduced solid-state microwave method as a newer and 'greener' synthetic methodology for the preparation of NiO nanoparticles [39]. This method has interesting features and might find application for the preparation of nanomaterials with improved properties which can provide considerable benefit in the fields of medicine. We also used this method for the preparation of Co-Sn-Cu oxides/graphene nanocomposites as green and recyclable catalysts for preparing 1,8-dioxo-octahydroxanthenes and apoptosis-inducing agents in MCF-7 human breast cancer [40]. The superiority of solid-state microwave method over the above mentioned conventional methods [8,41,42] for the synthesis of core-shell systems are reduction of physical and chemical cost, simplicity, safety, generation of pure nanoparticles as well as this method is green (no surfactant) and fast. Along this line, herein, we want to synthesize core-shell Fe<sub>3</sub>O<sub>4</sub>@SiO<sub>2</sub>@CuO nanocomposite by solid-state microwave method based on a novel nano-sized Fe<sub>3</sub>O<sub>4</sub>@SiO<sub>2</sub>@CuL precursor, prepared from the reaction of the Fe<sub>3</sub>O<sub>4</sub>@SiO<sub>2</sub> with a copper (II) Schiff base complex (CuL). Photocatalytic activity of the synthesized core-shell Fe<sub>3</sub>O<sub>4</sub>@SiO<sub>2</sub>@CuO nanocomposite was investigated for degradation of the cationic and anionic organic dye pollutants (MB and MO, respectively) under solar light. Also, this nanocomposite was applied as a new heterogeneous catalyst for the preparation of BIMs under mild conditions.

## 2. Experimental

### 2.1. General

The reagents and solvents were either prepared in our laboratory or were purchased from commercial suppliers Merck and Fluka. For the microwave irradiation, a microwave oven (LG: MH6535GISW, 1700 W, Korea) was used. Ultrasonic (US) generator was carried out on ultrasonic probe (Top-Sonics UPH-400, Germany). Proton nuclear magnetic resonance (<sup>1</sup>H NMR) spectra were recorded on 400 MHz spectrometer (Bruker, Germany) in deuterated chloroform. Fourier-transformed infrared spectroscopy (FT-IR) was used to obtain spectra of samples using a Shimadzu system FT-IR 8400 spectrophotometer (Japanese) by KBr pellets. X-ray diffraction (XRD) analysis was carried out using a Rigaku D-max C III, X-ray diffractometer with Ni-filtered Cu K $\alpha$  radiation (PANalytical X'Pert Pro, Netherlands). The morphology of samples was founded with field emission scanning electron microscopy (FESEM) that was taken on a Hitachi s4160/Japan with gold coating that was equipped with a link EDX analyzer. The magnetic property of the sample was measured by a vibrating sample magnetometer (VSM, Meghnatis Kavir Kashan Co., Kashan, Iran) at room temperature. UV-Vis spectra were measured on a double-beam Shimadzu 1650 PC UV-Vis (Japanese) and the samples were dispersed in 20 mL EtOH at room temperature for 20 min. Melting points were found out using a Fisher-Jones melting-point apparatus (USA).

Reaction monitoring was accomplished by thin layer chromatography (TLC) (silica gel 60-F250 precoated, England). Transmission electron microscopy (TEM) was imaged by Philips CM30 (Netherlands), a 300kV.

## 2.2. Preparation of the nano-sized $\text{Fe}_3\text{O}_4@\text{SiO}_2$

$\text{Fe}_3\text{O}_4$  magnetic nanoparticles were prepared by Fathirad's method [43]. Firstly, a solution of 20 mL  $\text{FeSO}_4 \cdot 2\text{H}_2\text{O}$  (1.6 g, aq.) and 50 mL  $\text{FeCl}_3 \cdot 6\text{H}_2\text{O}$  (3.8 g, aq.) was prepared. Then, 10 mL  $\text{NH}_3$  solution (25%) was slowly added to the above solution at the presence of ultrasonic irradiation (100 W) for 15 min under  $\text{N}_2$  atmosphere. After a few minutes, a black suspension was generated and then the  $\text{Fe}_3\text{O}_4$  magnetic nanoparticles were separated using an external permanent magnet. The nanoparticles were washed with distilled water, ethanol, and dried under vacuum at 70 °C. After the preparation of  $\text{Fe}_3\text{O}_4$  nanoparticles,  $\text{Fe}_3\text{O}_4@\text{SiO}_2$  structure was prepared by coating the  $\text{Fe}_3\text{O}_4$  nanoparticles with tetraethyl orthosilicate (TEOS). For this purpose, to 30 mL ethanolic suspension of the obtained  $\text{Fe}_3\text{O}_4$  was slowly added 4 mL TEOS. Then, 12 mL aqueous solution of ammonia (25 %) was added to this solution in the presence of ultrasonic irradiation (100 W) for 10 min. The dark brown precipitate,  $\text{Fe}_3\text{O}_4@\text{SiO}_2$ , was formed with stirring at room temperature after 24 h. The obtained  $\text{Fe}_3\text{O}_4@\text{SiO}_2$  was filtered off, washed with methanol, and dried under vacuum at room temperature.

## 2.3. Preparation of 4,4'-dibromo-2,2'-[cyclohexane-1,2-diylbis(nitrilomethanylylidene)]diphenol ( $\text{H}_2\text{L}$ )

To a 20 mL of methanolic solution of 5-bromosalicylaldehyde (0.4 g, 2 mmol) was added 1,2-diaminocyclohexane (0.1 g, 1 mmol) with continuous stirring. Then, the above solution was refluxed until a yellow precipitate was formed after 60 min. The precipitate was filtered, washed with methanol and ether, and dried under vacuum at 50 °C. The solid crude product was recrystallized from a solution of MeOH and DMF (2:1 in volume) to yield pure crystals of  $\text{H}_2\text{L}$  after several days [44].

## 2.4. Preparation of copper (II) Schiff base complex (CuL)

$\text{H}_2\text{L}$  ligand (0.3 mmol, 0.15 g), in methanol (10 mL), was exposed to ultrasonic irradiation (150 W). Afterwards, 10 mL methanolic solution of  $\text{Cu}(\text{CH}_3\text{COO})_2 \cdot 2\text{H}_2\text{O}$  (0.3 mmol, 0.14 g) was added dropwise to the above mixture, followed by 15 min sonication at room temperature. The mixture was filtered and the CuL powder (brown color) was washed successively with methanol and diethyl ether, and dried in air at ambient temperature overnight [45].

## 2.5. Preparation of the nano-sized $\text{Fe}_3\text{O}_4@\text{SiO}_2@\text{CuL}$ precursor

A suspension of  $\text{Fe}_3\text{O}_4@\text{SiO}_2$  (1 g) in chloroform (50 mL) was prepared by sonication and then excess amount of CuL Schiff base complex (1.2 g, 2 mmol) was added dropwise to the prepared suspension under ultrasonic irradiation for 30 min. The obtained dark brown suspension was stirred at room temperature for 12 h, afterwards the  $\text{Fe}_3\text{O}_4@\text{SiO}_2@\text{CuL}$  product was filtered off, washed twice with chloroform and diethyl ether, and dried under vacuum at room temperature overnight.

## 2.6. Preparation of the core-shell $\text{Fe}_3\text{O}_4@\text{SiO}_2@\text{CuO}$ nanocomposite

To prepare core-shell  $\text{Fe}_3\text{O}_4@\text{SiO}_2@\text{CuO}$  nanocomposite, 2 g of the  $\text{Fe}_3\text{O}_4@\text{SiO}_2@\text{CuL}$  precursor was poured into a porcelain crucible and it was placed in another bigger porcelain crucible, filled with CuO powder (as microwave irradiation absorber). The collection was placed in a microwave oven under microwaves irradiation in air (950 W, 350 °C). The generated heat led to the decomposition of precursor sample. After 10 min, decomposition of the  $\text{Fe}_3\text{O}_4@\text{SiO}_2@\text{CuL}$  precursor was completed. The  $\text{Fe}_3\text{O}_4@\text{SiO}_2@\text{CuO}$  nanocomposite product was washed with ethanol and dried under vacuum at room temperature overnight.

## 2.7. Photocatalytic tests

The photocatalytic ability of the core-shell  $\text{Fe}_3\text{O}_4@\text{SiO}_2@\text{CuO}$  nanocomposite was surveyed for the removal of MB or MO as organic dye pollutants from aqueous solutions. Firstly, the dosage of photocatalyst (0.004–0.007 mg), amount of  $\text{H}_2\text{O}_2$  (0–5 mL), and pH of the solution (5–10) were selected and optimized. The photocatalytic tests were performed on the days (10 AM to 2 PM) of bright sunny light (average light intensity of 180  $\text{mW cm}^{-2}$ ). Typically, 0.005 g of the  $\text{Fe}_3\text{O}_4@\text{SiO}_2@\text{CuO}$  nanocomposite as photocatalyst was added to 50 mL of MB or MO aqueous solution with concentration of 4 ppm and the mixture was stirred (500 rpm) at room temperature in dark for 30 min, in order to establish an adsorption–desorption equilibrium between catalyst and dye. Then, the mixture was exposed to solar light in the presence of an appropriate amount of  $\text{H}_2\text{O}_2$  (30%) at suitable pH, and consequently the degradation process of the dye took place. The degradation of MB and MO dyes was carried out at pH = 7 using 2 mL  $\text{H}_2\text{O}_2$  and at pH = 9 using 1 mL  $\text{H}_2\text{O}_2$ , respectively. At determined time intervals, the photocatalyst powder was isolated by centrifugation of 3 mL of the mixture and the degradation process of each dye was estimated by measuring the absorptions of MB and MO dyes at 663 and 462 nm, respectively, on their corresponding UV–Vis spectra. The pH of solution was adjusted to determined values by the dropwise addition of HCl (1 M) or NaOH (1 M) to the solution. The percent of degradation was measured by the following equation (Eq. (1)):

$$\text{Degradation (\%)} = \frac{C_0 - C_t}{C_0} \times 100, \text{ where } C_t \text{ is the final concentration of dye solution after a determined time (t) and } C_0 \text{ is the initial concentration of dye solution. After each experiment, the } \text{Fe}_3\text{O}_4@\text{SiO}_2@\text{CuO} \text{ nanocomposite was separated}$$

from the solutions by an external permanent magnet and then it was washed several times with water and ethanol and dried at 70 °C, and reused for the next experiments.

### 2.8. Typical procedure for the preparation of BIMs

A mixture of 2-thienyl carbaldehyde (1 mmol) and indole (2 mmol) was placed in a round-bottom flask containing 5 mL of EtOH/H<sub>2</sub>O (1:1). Subsequently, Fe<sub>3</sub>O<sub>4</sub>@SiO<sub>2</sub>@CuO nanocomposite catalyst (0.03 g) was added to the mixture and stirred at 80 °C. After the completion of the reaction as followed by TLC (chloroform), the catalyst was separated by an external permanent magnet. The remaining mixture was concentrated on a rotary evaporator under reduced pressure to give the desired product. The products were purified by recrystallization from ethanol or chromatographed on silica plates with chloroform as eluent where necessary.

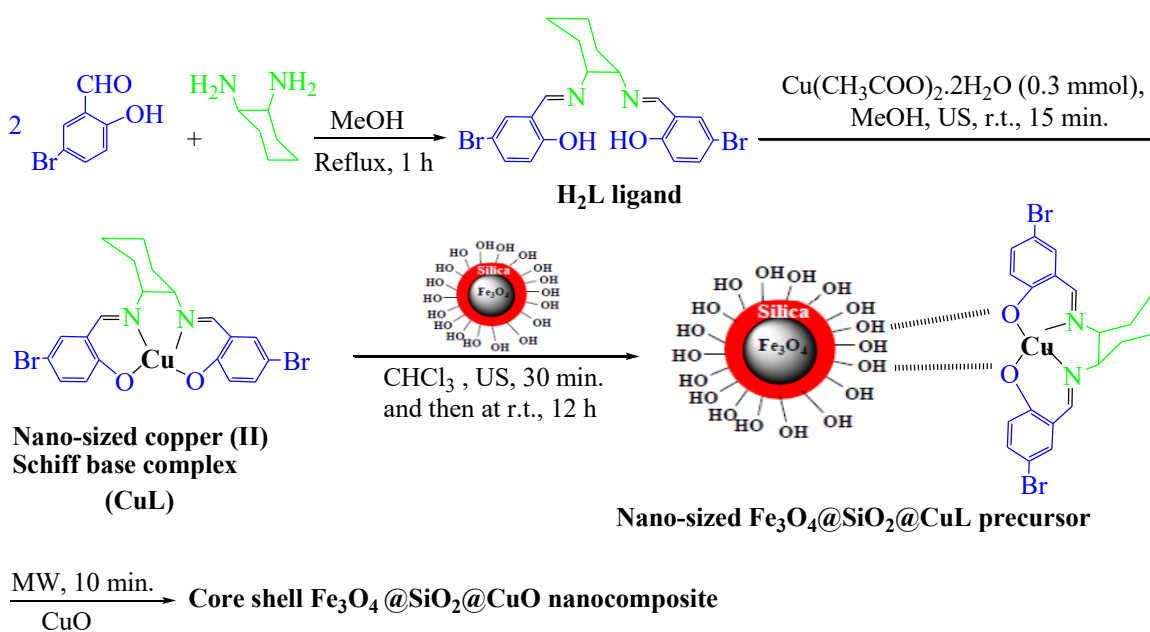
## 3. Results and discussion

### 3.1. Synthesis and structural characterization of nanocomposites

The core-shell Fe<sub>3</sub>O<sub>4</sub>@SiO<sub>2</sub>@CuO nanocomposite was prepared from Fe<sub>3</sub>O<sub>4</sub>@SiO<sub>2</sub>@CuL as a new precursor by solid-state microwave method (Scheme 2). In the first step, Fe<sub>3</sub>O<sub>4</sub> nanoparticles reacted with TEOS to afford the core-shell Fe<sub>3</sub>O<sub>4</sub>@SiO<sub>2</sub> [43]. In the second step, the nano-sized new copper (II) Schiff base complex (CuL) was synthesized from the chemical reaction of 1,2-diaminocyclohexane with 5-bromosalicylaldehyde, followed by the reaction with copper salt, Cu(CH<sub>3</sub>COO)<sub>2</sub>·2H<sub>2</sub>O, under ultrasonic irradiation [44,45]. Afterwards, Fe<sub>3</sub>O<sub>4</sub>@SiO<sub>2</sub>@CuL precursor was prepared from the treatment of Fe<sub>3</sub>O<sub>4</sub>@SiO<sub>2</sub> with CuL Schiff base complex under ultrasonic irradiation. In the next step, Fe<sub>3</sub>O<sub>4</sub>@SiO<sub>2</sub>@CuL precursor was exposed to microwave irradiation in order to be converted to core-shell Fe<sub>3</sub>O<sub>4</sub>@SiO<sub>2</sub>@CuO nanocomposite. However, the precursor remained unchanged for 30 min, which shows the compound cannot absorb microwaves. Therefore, it seems that attendance of microwave absorber is required. For this purpose, CuO powder was used as microwave irradiation absorber. By using CuO, we observed that the precursor was completely decomposed during the absorption of heat from the hot CuO and the nano-sized Fe<sub>3</sub>O<sub>4</sub>@SiO<sub>2</sub>@CuO powder was generated through the equation below (Eq. (2)) [46]. Note that in the synthesized core-shell Fe<sub>3</sub>O<sub>4</sub>@SiO<sub>2</sub>@CuO, Fe<sub>3</sub>O<sub>4</sub> is a magnetic core which increases magnetic property of particles and SiO<sub>2</sub> is chosen as an intermediary layer for the connection between shell layer (CuO) and the core (Fe<sub>3</sub>O<sub>4</sub>).



Figures 1a and 1b show the FT-IR spectra of the nano-sized CuL complex and Fe<sub>3</sub>O<sub>4</sub>@SiO<sub>2</sub>@CuL precursor, respectively. In Figure 1b, the band at 1609 cm<sup>-1</sup> was attributed to C=N group that show the red shift to lower frequency compared



US: Ultrasonic irradiation; MW: Microwave irradiation

**Scheme 2.** The synthetic routes for Fe<sub>3</sub>O<sub>4</sub>@SiO<sub>2</sub>@CuO nanocomposite.

with those of CuL complex ( $1640\text{ cm}^{-1}$ ) [45] as a result of the metal complex formation. The peaks at  $1095$  and  $466\text{ cm}^{-1}$  were assigned to Si–O and Fe–O bands, respectively [47]. By comparison of the IR spectrum of the nano-sized  $\text{Fe}_3\text{O}_4@/\text{SiO}_2@/\text{CuO}$  (Figure 1c) with  $\text{Fe}_3\text{O}_4@/\text{SiO}_2@/\text{CuL}$  precursor (Figure 1b), it will be clear that the bands of CuL complex were diminished and stretching frequencies of Si–O and Fe–O bands shifted toward  $1097$  and  $467\text{ cm}^{-1}$ , respectively. In addition, in Figure 1c, the distinct band at  $542\text{ cm}^{-1}$  was related to the Cu–O band in monoclinic phase [48] and the bands at  $1630$  and  $3300\text{--}3400\text{ cm}^{-1}$  could be assigned to the bending vibration and stretching vibration of  $\text{H}_2\text{O}$  absorbed by KBr pellets or the sample, respectively [45]. Thus, the IR spectral results indicate the successful decomposition of  $\text{Fe}_3\text{O}_4@/\text{SiO}_2@/\text{CuL}$  precursor by solid-state microwave method and formation of  $\text{Fe}_3\text{O}_4@/\text{SiO}_2@/\text{CuO}$  nanocomposite.

Figure 2 exhibits XRD analysis of the synthesized  $\text{Fe}_3\text{O}_4@/\text{SiO}_2@/\text{CuO}$  nanocomposite. The XRD result manifests the peaks of CuO in monoclinic phase (Space group: Cc, No: 9). The crystallographic parameters of a, b, and c are 4.69, 3.42

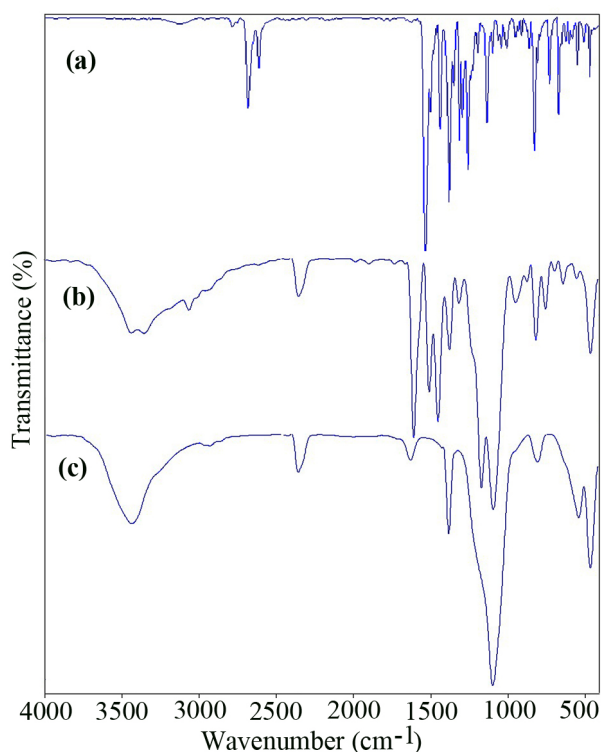


**Figure 1.** FT-IR spectra of the nano-sized CuL complex (a),  $\text{Fe}_3\text{O}_4@/\text{SiO}_2@/\text{CuL}$  precursor (b), and  $\text{Fe}_3\text{O}_4@/\text{SiO}_2@/\text{CuO}$  nanocomposite (c).

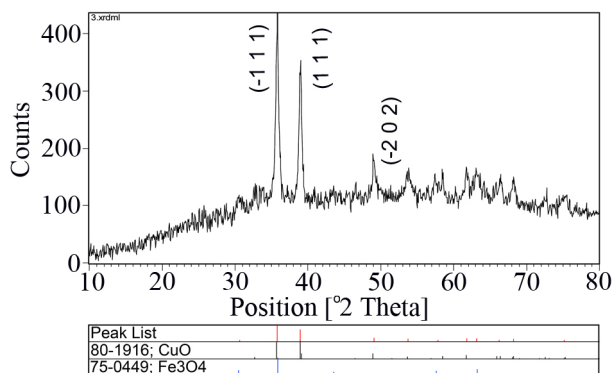


**Figure 2.** XRD pattern of the  $\text{Fe}_3\text{O}_4@/\text{SiO}_2@/\text{CuO}$  nanocomposite.

and 5.13 Å, respectively. Also, values of  $\alpha$ ,  $\beta$ , and  $\gamma$  parameters are 90.00°, 99.54°, and 90.00°, respectively. The significant peaks appeared at  $2\theta = 35.77^\circ$ ,  $38.95^\circ$ , and  $49.07^\circ$  that can be exactly related to  $(-1\ 1\ 1)$ ,  $(1\ 1\ 1)$ , and  $(-2\ 0\ 2)$  planes of crystal, respectively. In this pattern, only CuO (JCPDS Card No. 80-1916) and  $\text{Fe}_3\text{O}_4$  (JCPDS Card No. 75-0449) phases were observed. It is obvious that  $\text{SiO}_2$  have amorphous structure [49]. As shown in Figure 2, there are no peaks of impurity, suggesting that the pure crystalline  $\text{Fe}_3\text{O}_4@/\text{SiO}_2@/\text{CuO}$  was formed via solid state decomposition of  $\text{Fe}_3\text{O}_4@/\text{SiO}_2@/\text{CuL}$  precursor under microwave irradiation. Also, in the XRD pattern, wide width of the peaks is due to the formation of small size particles of the  $\text{Fe}_3\text{O}_4@/\text{SiO}_2@/\text{CuO}$  (Table 1). The mean size of the  $\text{Fe}_3\text{O}_4@/\text{SiO}_2@/\text{CuO}$  particles calculated by the Debye-Scherrer equation was found to be 23.83 nm [50].

The morphology of the synthesized  $\text{Fe}_3\text{O}_4@/\text{SiO}_2@/\text{CuL}$  precursor and  $\text{Fe}_3\text{O}_4@/\text{SiO}_2@/\text{CuO}$  nanocomposite were investigated by FESEM analysis. The images of the  $\text{Fe}_3\text{O}_4@/\text{SiO}_2@/\text{CuL}$  precursor were shown in Figures 3a and 3b at different magnification. As it can be seen, the morphology of the precursor is nanorod. However, from Figures 3c and 3d, it is clear that the morphology of  $\text{Fe}_3\text{O}_4@/\text{SiO}_2@/\text{CuO}$  particles are spherical shape and they are quite different from that of

**Table 1.** XRD data for the  $\text{Fe}_3\text{O}_4@/\text{SiO}_2@/\text{CuO}$  nanocomposite.

No.	1	2	3
POS [ $^\circ 2\text{TH}$ ]	35.77	38.95	49.07
FWHM [ $^\circ 2\text{TH}$ ]	0.38	0.32	0.38
hkl plane	$(-1\ 1\ 1)$	$(1\ 1\ 1)$	$(-2\ 0\ 2)$
Particle size (nm)	21.94	26.33	23.23

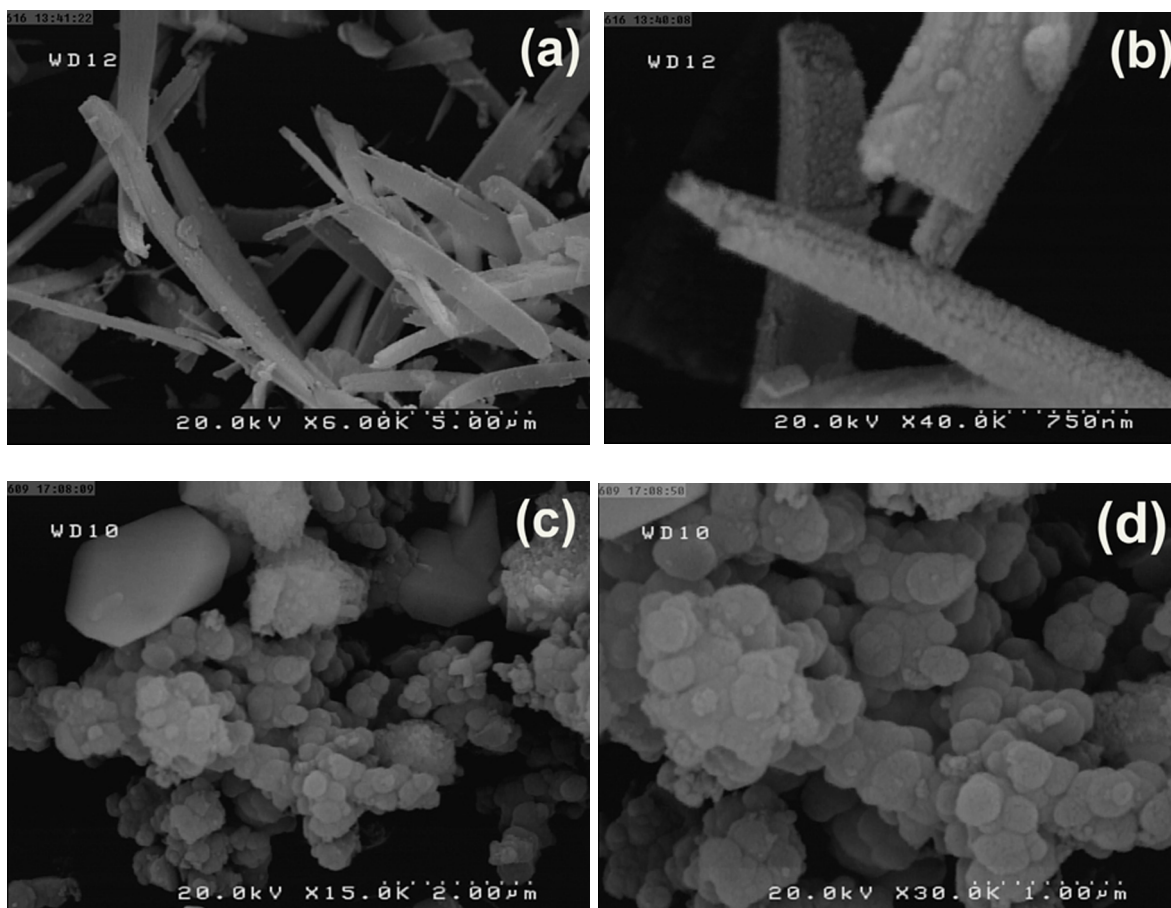


**Figure 3.** FESEM of the  $\text{Fe}_3\text{O}_4@/\text{SiO}_2@/\text{CuL}$  precursor (a,b) and  $\text{Fe}_3\text{O}_4@/\text{SiO}_2@/\text{CuO}$  nanocomposite (c,d) at different magnifications.

the precursor compound. Therefore, these results reveal that  $\text{Fe}_3\text{O}_4@\text{SiO}_2@\text{CuL}$  precursor was converted to  $\text{Fe}_3\text{O}_4@\text{SiO}_2@\text{CuO}$  particles by solid-state microwave method.

Figure 4a displays TEM analysis of the  $\text{Fe}_3\text{O}_4@\text{SiO}_2@\text{CuO}$  nanocomposite. A typical image of the synthesized sample shows core-shell shape of uniform nano crystalline structures. The black spot shows  $\text{Fe}_3\text{O}_4$  core which is surrounded by  $\text{SiO}_2$ . Also, ashen parts after  $\text{SiO}_2$  regions illustrate  $\text{CuO}$  shell. The particle size distribution of nanocomposite is 20–25 nm (Figure 4b). The particle size estimated by XRD diffraction pattern and the TEM analysis have good match with each other.

EDX spectrum of the core-shell  $\text{Fe}_3\text{O}_4@\text{SiO}_2@\text{CuO}$  nanocomposite is illustrated in Figure 5 and contains signals of Cu, Fe, Si, and, O elements. The Au and Si signals (notated as coating) were observed due to the instrument. Additionally, the weight and atomic percentages of the resided elements in obtained nanocomposite have been shown in a table inserted in Figure 5. Therefore, from the above results, it can again be concluded that  $\text{Fe}_3\text{O}_4@\text{SiO}_2@\text{CuO}$  nanocomposite was papered by solid-state microwaved method.

The alteration in magnetization (M) vs. applied field (H) for the core-shell  $\text{Fe}_3\text{O}_4@\text{SiO}_2@\text{CuO}$  nanocomposite at room temperature with field sweeping from  $-15,000$  to  $+15,000$  Oe is shown in Figure 6. The hysteresis loop shows a weak ferromagnetic behavior. The hysteresis loop of nano-sized materials was related to the magnetic anisotropy of the lattice, domain structure (pinning effect of magnetic domain walls at grain boundaries), as well as impurities within the nano-sized structures [51]. The remnant magnetization ( $M_r$ ) and saturation magnetization ( $M_s$ ) were found to be  $0.25$  and  $3.22$  emu  $\text{g}^{-1}$ , respectively. The value of coercive field ( $H_c$ ) was estimated as  $0.053$  Oe. The magnetic property of synthesized core-shell  $\text{Fe}_3\text{O}_4@\text{SiO}_2@\text{CuO}$  nanocomposite may be attributed to the different parameters such as sample shape, size, crystallinity, magnetization direction, and synthetic method.

The optical property of the prepared Schiff base complex CuL, nano-sized  $\text{Fe}_3\text{O}_4@\text{SiO}_2@\text{CuL}$  precursor, and core-shell  $\text{Fe}_3\text{O}_4@\text{SiO}_2@\text{CuO}$  nanocomposite was studied by UV–Vis spectroscopy. Figure 7a indicates the absorbance spectrum of the Schiff base complex CuL. The bands at  $200\text{--}300$  nm were due to  $\pi\text{--}\pi^*$  and  $n\text{--}\pi^*$  transitions. The band at around  $380$  nm was related to  ${}^2\text{B}_{1g} \rightarrow {}^2\text{E}_g$  transition at  $D_4h$  field [52]. In the  $\text{Fe}_3\text{O}_4@\text{SiO}_2@\text{CuL}$  spectrum (Figure 7b), the strong absorption band was observed at around  $250$  nm, which is due to the  $\pi\text{--}\pi^*$  transitions of the phenolic rings [53]. Also, the bands

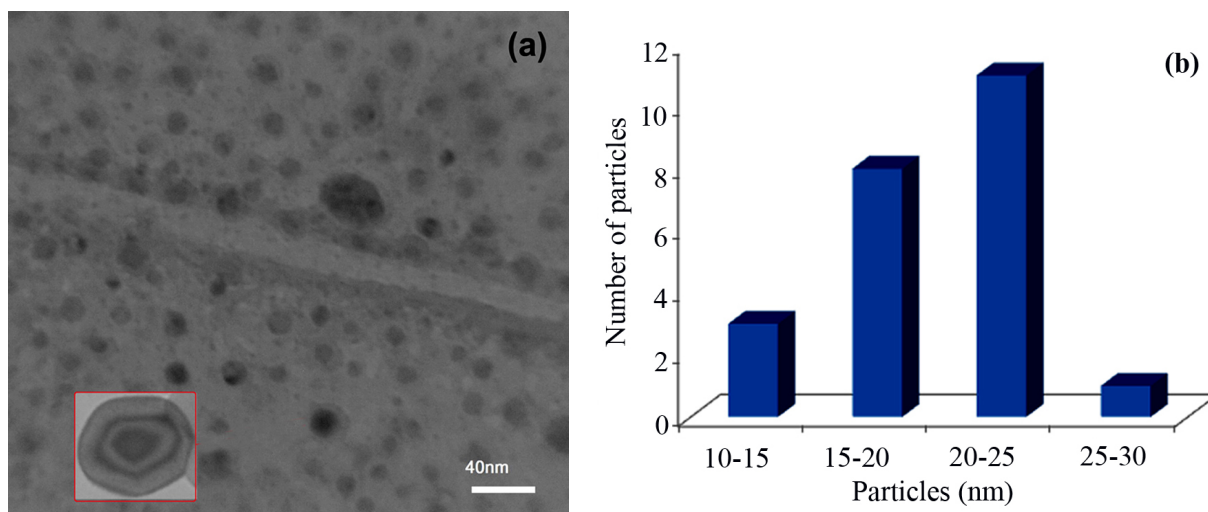


Figure 4. TEM image of core-shell  $\text{Fe}_3\text{O}_4@\text{SiO}_2@\text{CuO}$  nanocomposite (a) and particle size distribution (b).

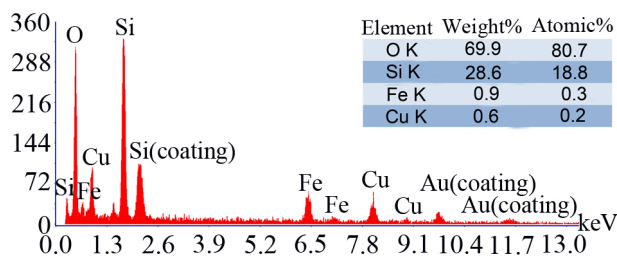
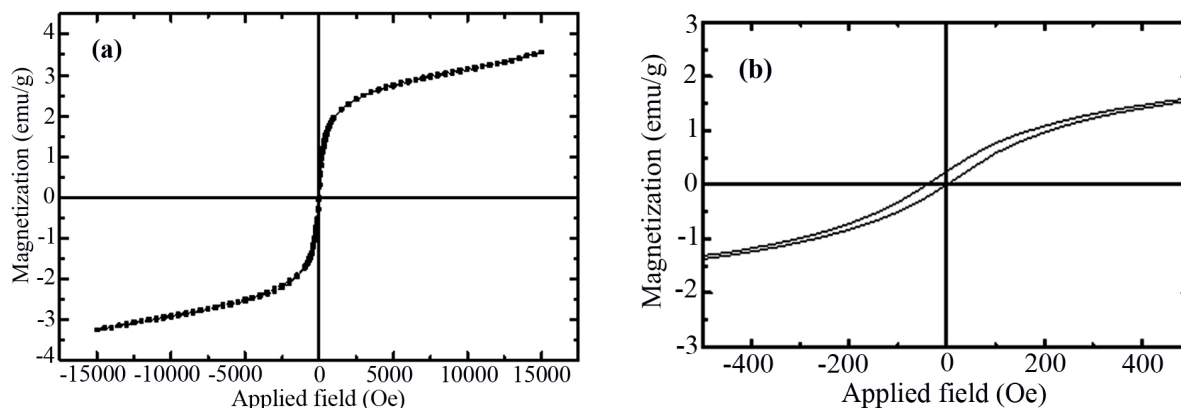


Figure 5. EDX spectrum of the  $\text{Fe}_3\text{O}_4@\text{SiO}_2@\text{CuO}$  nanocomposite.



**Figure 6.** Magnetization versus applied magnetic field for  $\text{Fe}_3\text{O}_4@\text{SiO}_2@\text{CuO}$  nanocomposite at room temperature (a) and enlarged view of the hysteresis loop in the low-field region (b).

appeared at 300–400 nm were related to the charge transfer transitions, MLCT and LMCT (metal ligand charge transfer and ligand metal charge transfer, respectively), which have shifted in comparison with those of CuL complex [45], due to the formation of  $\text{Fe}_3\text{O}_4@\text{SiO}_2@\text{CuL}$ . In Figure 7c, the bands observed are related to the electronic transition from Cu (3d) to O (2p) orbitals [54].

The band gap of the semiconductors can be calculated by Tauc's equation (Eq. (3)):  $(\alpha h\nu)^{1/n} = A(h\nu - E_g)$ , where  $\alpha$ ,  $h\nu$ ,  $A$ , and  $E_g$  are coefficient of absorption ( $\text{cm}^{-1}$ ), energy of photon (eV), proportionality constant, and the band gap energy (eV), respectively. The value of the exponent denotes the nature of the electronic transition (allowed or forbidden), and whether it is direct or indirect:  $n = 1/2$  for direct allowed transitions,  $n = 3/2$  for direct forbidden transitions,  $n = 2$  for indirect allowed transitions, and  $n = 3$  for indirect forbidden transitions. Plotting the  $(\alpha h\nu)^{1/n}$  versus  $(h\nu)$  is a matter of testing  $n = 1/2$  or  $n = 2$  to compare which provides the better fit and thus identifies the correct transition type. Figures 7d and 7e show curves of  $(\alpha h\nu)^2 - h\nu$  for the  $\text{Fe}_3\text{O}_4@\text{SiO}_2@\text{CuL}$  precursor and core-shell  $\text{Fe}_3\text{O}_4@\text{SiO}_2@\text{CuO}$  nanocomposite, respectively, showing a direct allowed transition. The linear region has been used to extrapolate to the X-axis intercept to find the  $E_g$  value. Using this concept, the  $E_g$  values of  $\text{Fe}_3\text{O}_4@\text{SiO}_2@\text{CuL}$  precursor and core-shell  $\text{Fe}_3\text{O}_4@\text{SiO}_2@\text{CuO}$  nanocomposite were found to be 4.7 and 3.2 eV, respectively.  $E_g$  values of  $\text{Fe}_3\text{O}_4$  and  $\text{Fe}_3\text{O}_4@\text{SiO}_2$  have been found to be 1.3 and 1.68 eV, respectively [55]. As it can be seen,  $E_g$  of core-shell  $\text{Fe}_3\text{O}_4@\text{SiO}_2@\text{CuO}$  nanocomposite has shifted in comparison with those of  $\text{Fe}_3\text{O}_4@\text{SiO}_2@\text{CuL}$  precursor. The band of core-shell  $\text{Fe}_3\text{O}_4@\text{SiO}_2@\text{CuO}$  nanocomposite shows red shift toward CuO thin films [56] or blue shift in comparison with quantum dots of CuO [57]. This difference is probably related to morphology, size, and effect of the present elements or synthetic method.

Because of a moderate band gap (3.2 eV) of core-shell  $\text{Fe}_3\text{O}_4@\text{SiO}_2@\text{CuO}$  nanocomposite, we anticipated that it can act as a photocatalyst for destroying the dye pollutants. For this purpose, the photocatalytic activity of core-shell  $\text{Fe}_3\text{O}_4@\text{SiO}_2@\text{CuO}$  nanocomposite was investigated for solar light degradation of MB and MO organic dye pollutants. Firstly, the experiments were carried out for degradation of MB as a typical cationic dye. The degradation of MB dye was investigated at 663 nm at which the dye shows a strong absorption. Figure 8a shows the values of  $C_t/C_0$  of MB dye in different conditions. Clearly, the  $C_t/C_0$  values under the optimized conditions (pH= 7 and 2 mL of  $\text{H}_2\text{O}_2$ ) strongly decreased at room temperature due to the solar light degradation process. The  $\text{H}_2\text{O}_2$  acts as an assisted-degradation and produces more free radicals ( $\text{HO}\cdot$ ), which leads to faster and more effective degradation. However, use of further amounts of hydrogen peroxide, up to critical concentration, will not enhance the rate of dye degradation process [58].

The characteristic absorption bands of MB dye at optimized conditions at 663 nm at different times are given in Figure 8b. Clearly, the characteristic absorption decreases with the passage of time. The absorption of MB is about zero after 180 s solar light irradiation. During the degradation process, the intense blue color of the initial solution was decreased until it becomes almost colorless, indicating the successful solar light degradation process of MB. It is worth noting that the absorption bands of MB were not shifted at 663 nm, denoting that the degradation of MB is due to the degradation of the chromophore groups [59]. Thus, the core-shell  $\text{Fe}_3\text{O}_4@\text{SiO}_2@\text{CuO}$  nanocomposite is an efficacious photocatalyst for the degradation of MB dye in short time with a degradation efficiency of 97 %. In order to demonstrate the effectiveness of photons in dye degradation processes, typically, 0.005 g of the  $\text{Fe}_3\text{O}_4@\text{SiO}_2@\text{CuO}$  nanocomposite was added to 50 mL of MB or MO aqueous solution with concentration of 4 ppm and the mixture was stirred (500 rpm) at room temperature in dark for 30 min. UV-Vis spectra showed that the significant absorption peaks of dyes were observed without decreasing. Therefore, dye degradation is accomplished in the presence of light.



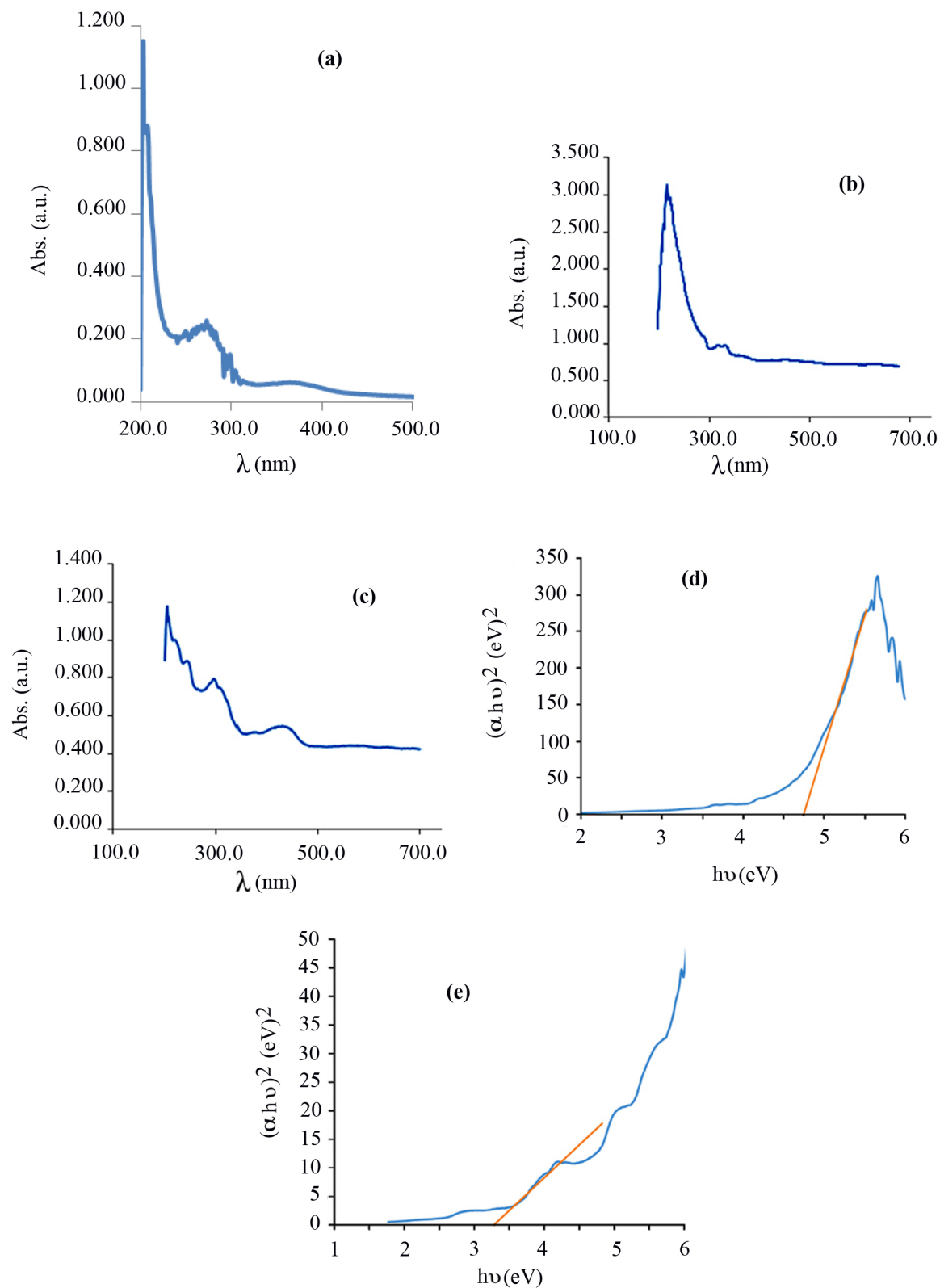


**Figure 7.** Electronic spectra of Schiff base complex CuL (a), the  $\text{Fe}_3\text{O}_4@SiO_2@CuL$  precursor (b), and core-shell  $\text{Fe}_3\text{O}_4@SiO_2@CuO$  nanocomposite (c) and  $(\alpha h\nu)^2 - h\nu$  curves of the  $\text{Fe}_3\text{O}_4@SiO_2@CuL$  precursor (d) and core-shell  $\text{Fe}_3\text{O}_4@SiO_2@CuO$  nanocomposites (e).

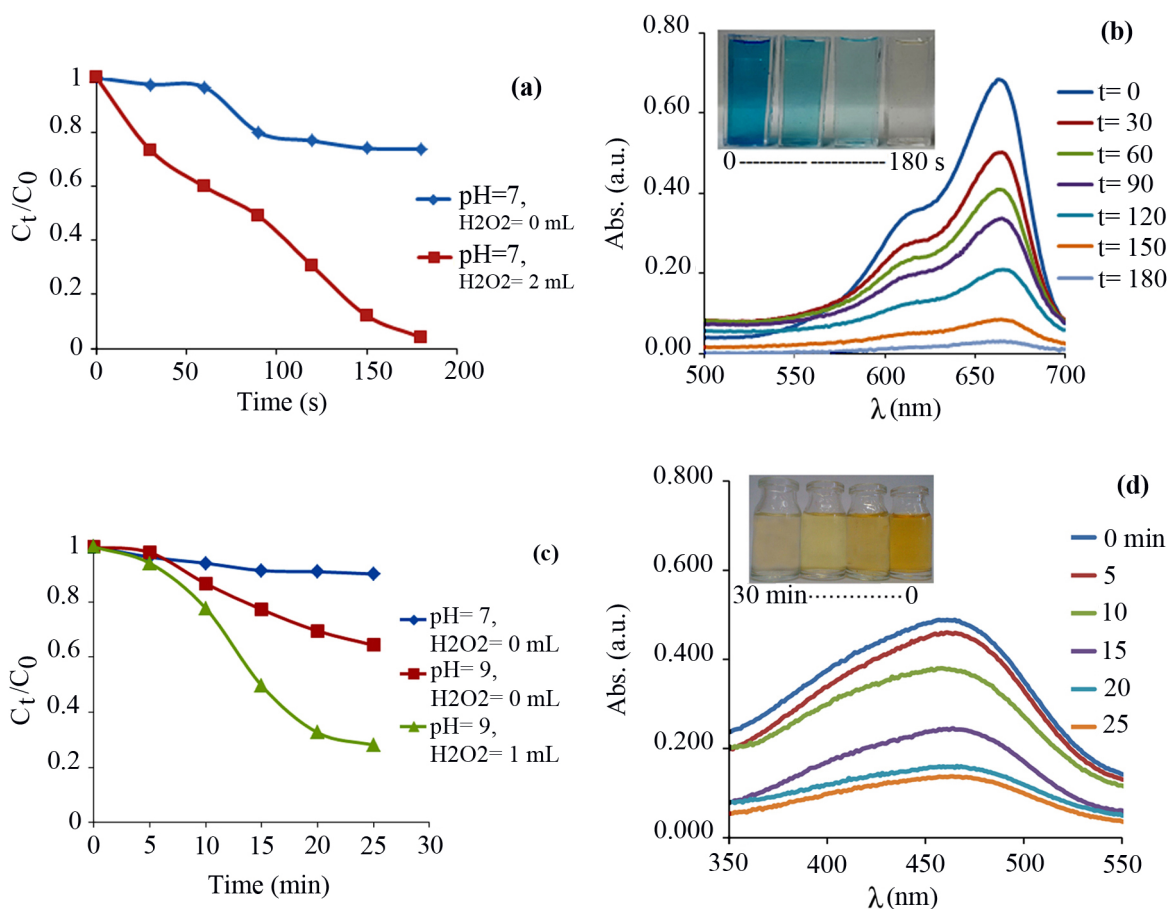


**Figure 8.** Concentration changes ( $C_t/C_0$ ) versus irradiation time and time-dependent absorption spectrum during degradation process of a 4 ppm aqueous solution of MB (a,b, respectively) and MO (c,d, respectively) dyes in the presence of the core-shell  $Fe_3O_4@SiO_2@CuO$  nanocomposite (0.005 g) as a photocatalyst.

Based on this encouraging result, the core-shell  $Fe_3O_4@SiO_2@CuO$  nanocomposite was subsequently extended to the degradation of MO as a typical anionic dye in similar conditions. The experimental tests showed that the values of  $C_t/C_0$  of MO dye under optimized conditions (pH = 9 and 1 mL of  $H_2O_2$ ) decreased sharply at room temperature (Figure 8c). The intensity change of the absorption bands at 462 nm over of the  $Fe_3O_4@SiO_2@CuO$  nanocomposite catalyst is plotted in Figure 8d as a function of time. After 25 min, the degradation efficiency for MO was estimated as 72 %. When the results obtained for the degradation of MB and MO dyes using the  $Fe_3O_4@SiO_2@CuO$  nanocomposite were compared with each other, it was revealed that the degradation of MB dye (the cationic dye) was performed with higher yield in a shorter time, which indicates that the surface of the  $Fe_3O_4@SiO_2@CuO$  nanocomposite catalyst is presumably negatively charged.

A radical mechanism for the solar light degradation of MB or MO dyes over core-shell  $Fe_3O_4@SiO_2@CuO$  nanocomposite is proposed in Figure 9 [55]. During irradiation,  $Fe_3O_4@SiO_2@CuO$  nanocomposite ( $E_g = 3.2$  eV) can create electron-hole pairs (Eq. (4)). The electrons on the conductive band (CB) react with  $H_2O_2$  molecules to produce  $HO\cdot$  and  $\bullet O_2^-$  radicals (Eqs. 5 and 6). Meanwhile, holes on the valence band (VB) would be reacted with the  $H_2O$  molecules or  $OH^-$  ions to form  $HO\cdot$  radicals (Eq. (7)). The produced active  $HO\cdot$  and  $\bullet O_2^-$  radicals effectively degrade the dye molecules to  $CO_2$ ,  $H_2O$  and other inorganic products (Eqs. (8) and (9)).



The solar light degradation kinetics of MB (Figure 10a) and MO (Figure 10b) dyes were determined. The pseudo-zero order model was used:  $C_t = -k_t + C_0$ , where  $C_0$  and  $C_t$  are the dye concentrations before and after solar light irradiation, respectively,  $t$  is the reaction time as well as  $k$  is the rate constant. As shown in Figure 10, the  $k$  values for the degradation of MB and MO dyes were found to be  $3.6 \times 10^{-3} \text{ s}^{-1}$  and  $0.213 \times 10^{-3} \text{ s}^{-1}$ , respectively. The results indicate that the MB degradation rate is more than those of MO dye. The  $k$  value for the photodegradation of MB dye using the  $\text{Fe}_3\text{O}_4$  nanoparticles has been found to be  $1.7 \times 10^{-4} \text{ s}^{-1}$  [60], lower than that of  $\text{Fe}_3\text{O}_4@\text{SiO}_2@\text{CuO}$  nanocomposite ( $3.6 \times 10^{-3} \text{ s}^{-1}$ ), thus, the latter ones seem to be more effective for dye degradation process.

One of the important issues in the catalytic experiments is stability and reusability of the catalysts. The synthesized core-shell  $\text{Fe}_3\text{O}_4@\text{SiO}_2@\text{CuO}$  nanocomposite is a magnetic material and after each reaction it was easily segregated using an external permanent magnet. After washing core-shell  $\text{Fe}_3\text{O}_4@\text{SiO}_2@\text{CuO}$  nanocomposite severally with deionized water, the solid was dried and reused for consecutive cycles for the degradation of MB or MB dyes. The results showed that  $\text{Fe}_3\text{O}_4@\text{SiO}_2@\text{CuO}$  nanocomposite can be reused up to five cycles with no significant decline in degradation efficiency (Figure 11a). Negligible loss in its activity is due to loss of catalyst during separation or through washing cycles. These results were authenticated with FESEM and EDX spectra of  $\text{Fe}_3\text{O}_4@\text{SiO}_2@\text{CuO}$  nanocomposite after fifth reuse (Figures 11b and 11c), indicating that the structure of the catalyst was preserved after recovery.

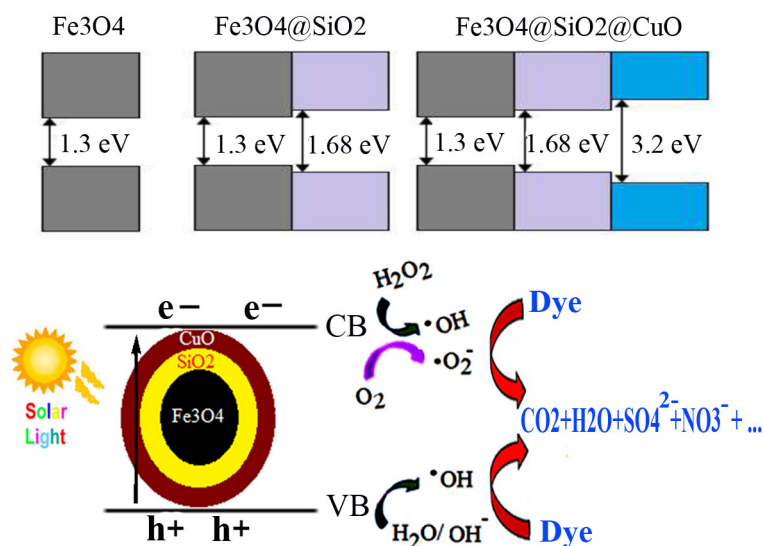


**Figure 9.** A proposed mechanism of solar light degradation of MB or MO dyes in aqueous solution over the core-shell  $\text{Fe}_3\text{O}_4@\text{SiO}_2@\text{CuO}$  nanocomposite/ $\text{H}_2\text{O}_2$  system with an energy level diagram. CB and VB are the conduction and the valence bands, respectively.

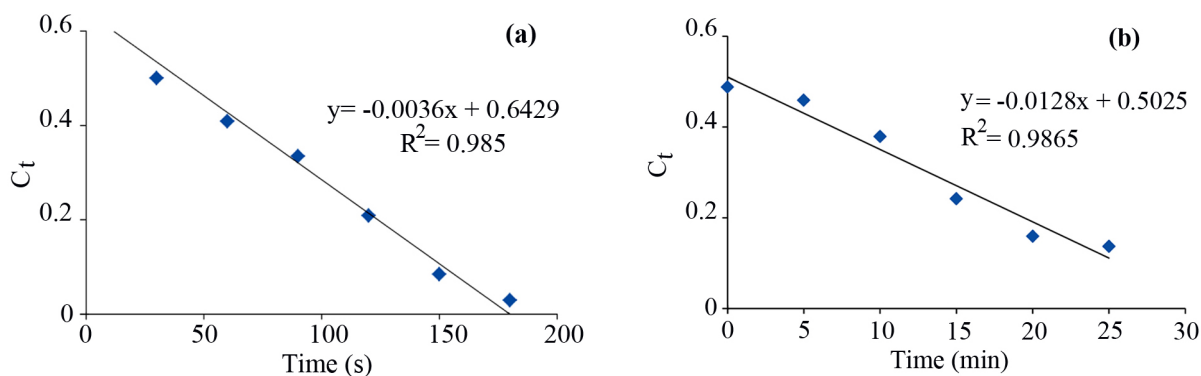


**Figure 10.** Plot of  $C_t$  versus irradiation time for MB (a) and MO (b) dyes over  $\text{Fe}_3\text{O}_4@\text{SiO}_2@\text{CuO}$  nanocomposite. The removal of dyes by this nanocomposite followed pseudo-zero order kinetics.

Finally, the photocatalytic performance of the synthesized core-shell  $\text{Fe}_3\text{O}_4@\text{SiO}_2@\text{CuO}$  nanocomposite, for degradation of MB and MO dye pollutants was compared with previously reported literature (Table 2). The results showed that  $\text{Fe}_3\text{O}_4@\text{SiO}_2@\text{CuO}$  nanocomposite provides better catalytic performances than the previously reported photocatalysts from view of the degradation efficiency and reaction rate. Notably, whereas many catalysts used for the degradation of dyes (entries 1–6) require an additional energy (UV irradiation, ultrasound or microwave source) or heating conditions,  $\text{Fe}_3\text{O}_4@\text{SiO}_2@$

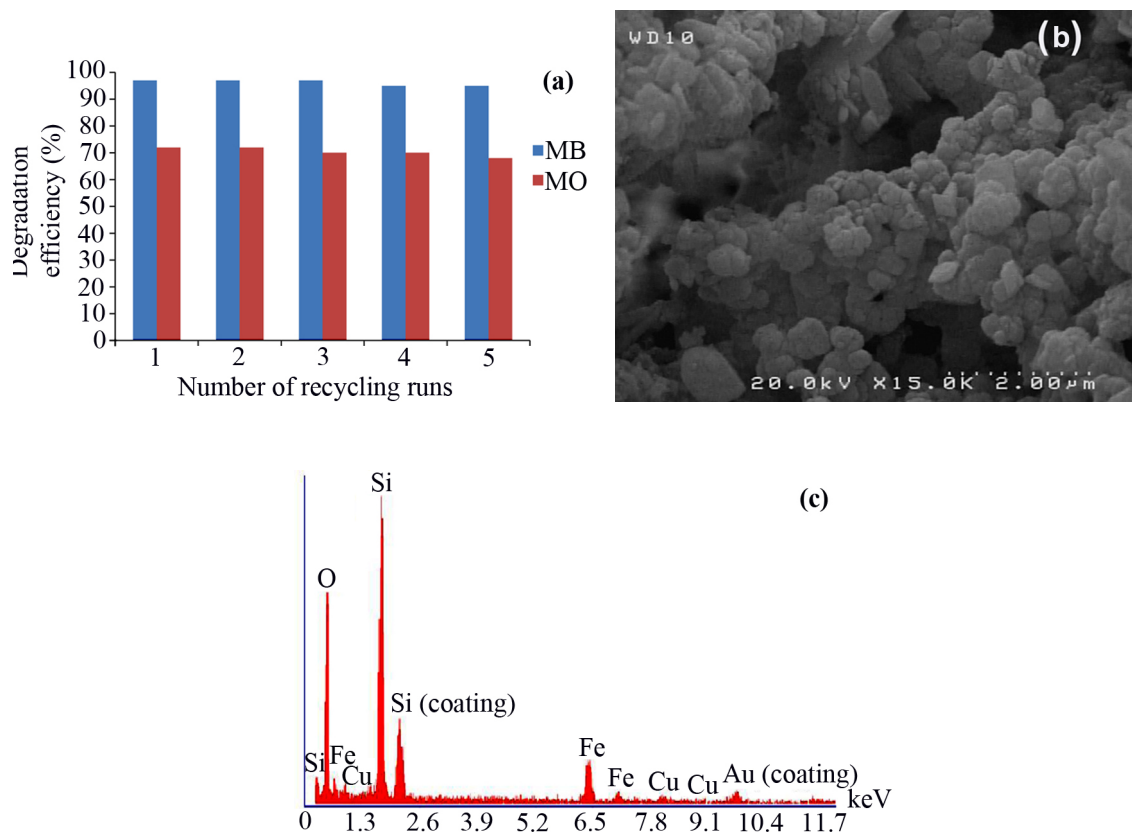


**Figure 11.** Reusability of core-shell  $\text{Fe}_3\text{O}_4@\text{SiO}_2@\text{CuO}$  nanocomposite (0.005 g) in the degradation of a 4 ppm aqueous solution of MB and MO dyes after 3 and 25 min, respectively, (a), its FESEM image (b) and EDX spectrum (c) after fifth reuse.

**Table 2.** Comparing the photocatalytic efficiency of core-shell  $\text{Fe}_3\text{O}_4@\text{SiO}_2@\text{CuO}$  nanocomposite with some previously reports in degradation of organic dye pollutants.

No.	Nanomaterial	Dye	Irradiation	Degradation efficiency (%)	Time (min)	Synthetic method
1	CuO	MO	UV	12	120	Precipitation [61]
2	$\text{Fe}_3\text{O}_4@\text{CuO}$ -RGO	MB	UV	94	150	Hydrothermal [62]
3	$\text{Mn}_3\text{O}_4$	MB	Heat	82	24	Sol-gel [63]
4	$\text{ZnFe}_2\text{O}_4$	MB	MW <sup>a</sup>	32	30	MW <sup>a</sup> sintering [64]
5	MIL-101(Cr)/RGO <sup>b</sup> / $\text{ZnFe}_2\text{O}_4$	MB	US <sup>c</sup>	96	50	Hydrothermal [65]
6	MIL-101(Cr)/RGO <sup>b</sup> / $\text{ZnFe}_2\text{O}_4$	MO	US <sup>c</sup>	80	70	Hydrothermal [65]
7	Core-shell $\text{Fe}_3\text{O}_4@\text{SiO}_2@\text{CuO}$	MB	Solar light	97	3	MW <sup>a</sup> decomposition
8	Core-shell $\text{Fe}_3\text{O}_4@\text{SiO}_2@\text{CuO}$	MO	Solar light	72	25	MW <sup>a</sup> decomposition

<sup>a</sup> Microwave, <sup>b</sup> reduced graphene oxide, <sup>c</sup> ultrasound.

CuO nanocomposite does not need an external energy and the degradation process of dyes was carried out only under solar energy. Noteworthy is that in a recent work [66], nanoplate of mixed- $\text{Fe}_3\text{O}_4@\text{SiO}_2@\text{CuO}$  synthesized by precipitation method was reported as a photocatalyst for destroying the MO dye. However, the degradation efficiency was low (17.6%) and the degradation process could be accomplished only under UV-Vis irradiation. The superiority of our core-shell  $\text{Fe}_3\text{O}_4@\text{SiO}_2@\text{CuO}$  nanocomposite over nanoplate of mixed- $\text{Fe}_3\text{O}_4@\text{SiO}_2@\text{CuO}$  seems to depend on the differences in morphology and type of precursor, and also applied synthetic method. In the solid-state microwave decomposition method, at the molecular level, microwaves interact with the reactants and the electromagnetic energy is generated. This energy change to heat by rapid kinetics of the molecules and can improve the chemical reaction [39].

Encouraged by the results obtained from the photocatalytic efficiency of  $\text{Fe}_3\text{O}_4@\text{SiO}_2@\text{CuO}$  in degradation of organic dye pollutants, we turned our attention to examine the catalytic activity of this nanocomposite for the preparation of

**Table 3.** Preparation of BIMs.

No.	R	Time (min)	Yield (%) <sup>a</sup>	M.p (°C) (Lit. [Ref])
1		20	96	123–127 (126–127) [23]
2		11	97	216–220 (218–220) [36]
3		12	95	214–218 (220–222) [36]
4		12	94	211–215 (209–211) [23]
5		18	96	78–82 (77–78) [29]
6		20	95	113–117 (112–113) [23]
7		16	96	105–110 (100–102) [29]
8		22	93	315–318 (321–322) [36]
9		20	97	147–150 (151–153) [22]
10		28	93	185–187 (187–189) [22]
11		25	93	93–96 (95–97) [23]
12		30	92	70–73 (68–70) [21]
13		120	trace	-

<sup>a</sup> Isolated yield. All products are known compounds and were identified by comparison of their physical and spectral data with those of the authentic samples.

BIMs. Catalytic experiments were initiated with the reaction of 2-thienyl carbaldehyde (1 equiv.) with indole (2 equiv.) as a typical reaction. To find the optimum reaction conditions, the influence of the solvent nature, reaction temperature, and amount of catalyst were investigated. The best yields were obtained in EtOH/H<sub>2</sub>O (1:1) at 80 °C in the presence of 0.03 g of Fe<sub>3</sub>O<sub>4</sub>@SiO<sub>2</sub>@CuO nanocomposite. After this, the performance of this approach was explored for the preparation of a wide variety of BIMs. BIMs were obtained in excellent yields using Fe<sub>3</sub>O<sub>4</sub>@SiO<sub>2</sub>@CuO nanocomposite from various aliphatic and aromatic aldehydes, having different substituents, and indole (Table 3, entries 1–7, 10–12). Also, heteroaromatic aldehydes smoothly reacted with indole using Fe<sub>3</sub>O<sub>4</sub>@SiO<sub>2</sub>@CuO nanocomposite to yield their corresponding BIMs (entries 8,9). Reaction of ketones with indole was very slow (entry 13) due to steric effects, and the product was afforded only in trace amounts even after extended time (120 min). In all cases, the reaction proceeds smoothly without the formation of any undesirable products, which normally are observed under the influence of strong acid catalysts. The work-up is reduced to a mere separation of the magnetic catalyst and evaporation of the solvent. Figure 12 shows the <sup>1</sup>H NMR spectrum of the 3,3'-(2-thienylmethylene)bis-1H-indole (as a brick red powder).

To explore the actual role of Fe<sub>3</sub>O<sub>4</sub>@SiO<sub>2</sub>@CuO nanocomposite in the synthesis of BIMs, we explain a plausible mechanism of the reaction in Scheme 3. An activated aldehyde carry out an electrophilic substitution reaction at C-3 of an indole, which after loss of water yields intermediate I. Addition of another molecule of indole to intermediate I, like the Michael addition fashion, yields intermediate II, which produces the target product after aromatization takes place via deprotonation.

The reusability of the Fe<sub>3</sub>O<sub>4</sub>@SiO<sub>2</sub>@CuO nanocomposite catalyst in the synthesis of BIMs was studied. The catalyst was reused up to five times without remarkable loss of its efficiency (Figure 13).

A comparison of the present procedure, using Fe<sub>3</sub>O<sub>4</sub>@SiO<sub>2</sub>@CuO nanocomposite, with selected previously reported catalysts is presented in Table 4. Clearly, Fe<sub>3</sub>O<sub>4</sub>@SiO<sub>2</sub>@CuO nanocomposite in addition to having the advantages such as easy separation and recyclability has fine catalytic performance compared to other reported protocols.

#### 4. Conclusion

In summary, well-defined core-shell Fe<sub>3</sub>O<sub>4</sub>@SiO<sub>2</sub>@CuO composite was prepared via a fast and efficient solid state microwave irradiation. The composite is a ferromagnetic material in the nano scale range of size (20–25 nm) with a moderate band gap

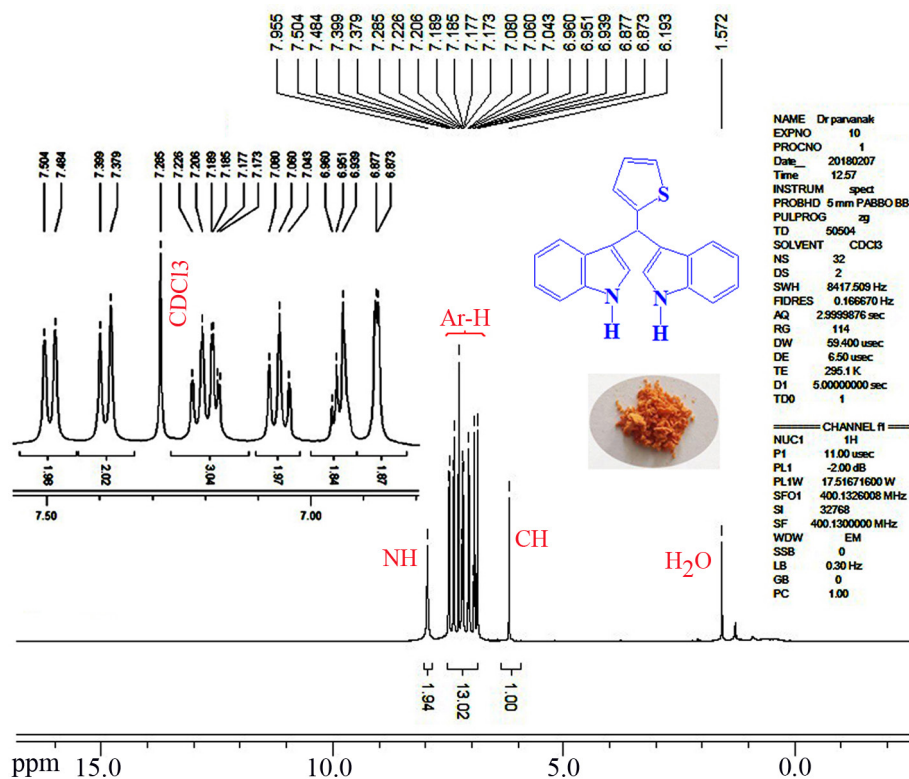
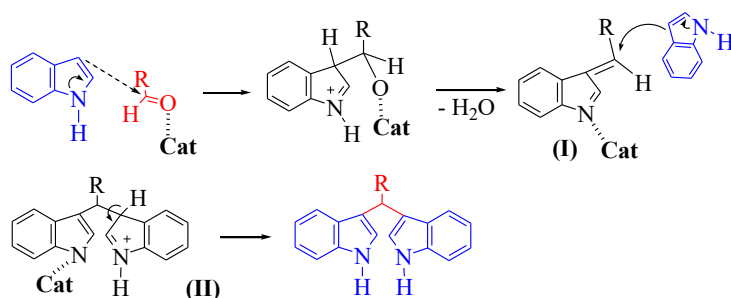
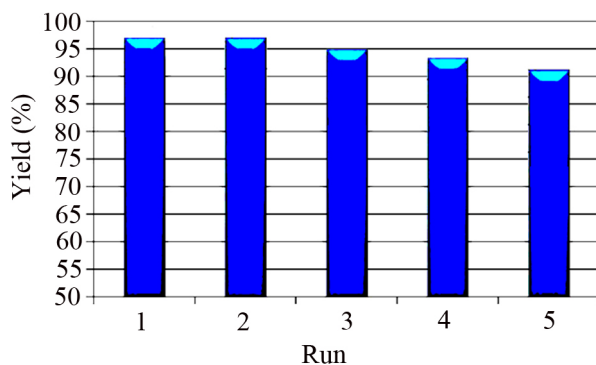


Figure 12. <sup>1</sup>H NMR spectrum of the 3,3'-(2-thienylmethylene)bis-1H-indole in CDCl<sub>3</sub> as solvent.



**Scheme 3.** A probable mechanism of the reaction of aldehydes with indole in the presence of  $\text{Fe}_3\text{O}_4@\text{SiO}_2@\text{CuO}$  nanocomposite as catalyst.



**Figure 13.** Recyclability of  $\text{Fe}_3\text{O}_4@\text{SiO}_2@\text{CuO}$  nanocomposite (0.03 g) in the reaction of 2-thienyl carbaldehyde (1 mmol) with indole (2 mmol) in EtOH/H<sub>2</sub>O (1:1) at 80 °C after 20 min.

**Table 4.** Comparison of the efficiencies of  $\text{Fe}_3\text{O}_4@\text{SiO}_2@\text{CuO}$  nanocomposite with other reported catalysts for the condensation of indole with benzaldehyde.

No.	Cat.	Solv.	Temp. (°C)	Time (min)	Yield (%) <sup>a</sup>
1	InCl <sub>3</sub>	MeCN	r.t.	240	96 [20]
2	LiClO <sub>4</sub>	MeCN	r.t.	300	90 [21]
3	I <sub>2</sub>	solvent-free	r.t.	10	72 [22]
4	Sulfamic acid	solvent-free	r.t.	92	30 [23]
5	HBF <sub>4</sub> -SiO <sub>2</sub>	solvent-free	r.t.	10	94 [24]
6	PEG-sulfonic acid	MeOH	r.t.	150	95 [25]
7	Sulfonated polyacrylamide	MeCN	reflux	60	95 [26]
8	SiO <sub>2</sub> -AlCl <sub>3</sub>	solvent-free	r.t.	35	96 [27]
9	Nafion-H <sup>+</sup>	PEG/H <sub>2</sub> O	80 °C	25	94 [28]
10	[DABCO-H][HSO <sub>4</sub> ]	neat	90 °C	120	91 [29]
11	Nano <i>n</i> -propylsulfonated $\gamma\text{-Fe}_2\text{O}_3$	solvent-free	80 °C	60	82 [30]
12	Sc(OTf) <sub>3</sub>	THF	r.t.	210	92 [31]
13	CaO	solvent-free	100 °C	210	70 [32]
14	Graphene oxide	H <sub>2</sub> O	40 °C	180	92 [33]
15	MBS	neat	r.t.	60	86 [34]
16	HCP@CH <sub>2</sub> Br	neat	60 °C	60	96 [35]
17	Itaconic acid	H <sub>2</sub> O	100 °C	120	90 [36]
18	Borophosphate glasses	solvent-free	70 °C	90	94 [37]
19	Fe <sub>3</sub> O <sub>4</sub> @sucrose-OBF <sub>3</sub> H	EtOAc	70 °C	150	92 [38]
20	Fe <sub>3</sub> O <sub>4</sub> @SiO <sub>2</sub> @CuO	EtOH/H <sub>2</sub> O	80 °C	20	96

<sup>a</sup> Isolated yields.

of 3.2 eV, which makes it suitable for applications in areas such as electronics and photonics. The MB and MO dyes were degraded over  $\text{Fe}_3\text{O}_4@\text{SiO}_2@\text{CuO}$  nanocomposite as a reusable photocatalyst with 97% and 72% efficiency, respectively. The important feature of the present protocol was the use of solar energy to accomplish the degradation of dye pollutants. Also, the nanocomposite exhibited high catalytic activity in the BIMs synthesis. The catalyst is easily separable by an external magnet and its catalytic activity remains after several reaction cycles. The cleaner reaction profiles, simple work-up, no competitive side reactions, high reaction rates, and high yields of the desired products are other advantages of this method. The synthesis and applications of other core-shell nanocomposites with different magnetic cores using solid state microwave method is under investigation.

### Conflict of interest

The authors have no conflicts of interest to declare.

### Acknowledgment

The author thanks the Research Council of Shahrekord University and Islamic Azad University, Shahrekord Branch for their partial support of this work.

### References

1. Li W, Mu B, Yang Y. Feasibility of industrial-scale treatment of dye waste water via bio-adsorption technology. *Bioresource Technology* 2019; 277: 157–170. doi: 10.1016/j.biortech.2019.01.002
2. Jiang X, Xia H, Zhang L, Peng J, Cheng S et al. Ultrasound and microwave-assisted synthesis of copper-activated carbon and application to organic dyes removal. *Powder Technology* 2018; 338: 857–868. doi: 10.1016/j.powtec.2018.07.089
3. Molla A, Li Y, Mandal B, Kang SG, Hur SH et al. Selective adsorption of organic dyes on graphene oxide: Theoretical and experimental analysis. *Applied Surface Science* 2019; 464: 170–177. doi: 10.1016/j.apsusc.2018.09.056
4. Hu H, Lin Y, Hu YH. Core-shell structured  $\text{TiO}_2$  as highly efficient visible light photocatalyst for dye degradation. *Catalysis Today* 2020; 341: 90–95. doi: 10.1016/j.cattod.2019.01.077
5. Wang P, Qi C, Hao L, Wen P, Xu X. Sepiolite/ $\text{Cu}_2\text{O}/\text{Cu}$  photocatalyst: preparation and high performance for degradation of organic dye. *Journal of Materials Science & Technology* 2019; 35 (3): 285–291. doi: 10.1016/j.jmst.2018.03.023
6. Boikanyo D, Masheane ML, Nthunya LN, Mishra SB, Mhlanga SD. Carbon-supported photocatalysts for organic dye photodegradation. In: Mustansar Hussain C, Kumar Mishra A (editors). *New Polymer Nanocomposites for Environmental Remediation*. New York: Elsevier BV, 2018, pp. 99–138. doi: 10.1016/B978-0-12-811033-1.00005-6
7. Kisala J, Hęclic K, Masłowska A, Celuch M, Pogocki D. Natural environments for nanoparticles synthesis of metal, metal oxides, core-shell and bimetallic systems. In: Rahman AU (editor). *Studies in Natural Products Chemistry*. New York: Elsevier BV, 2017, vol. 52, pp. 1–67. doi: 10.1016/B978-0-444-63931-8.00001-1
8. Chen W, Yan RQ, Chen GH, Chen MY, Huang GB et al. Hydrothermal route to synthesize helical  $\text{CdS}/\text{ZnIn}_2\text{S}_4$  core-shell heterostructures with enhanced photocatalytic hydrogen generation activity. *Ceramics International* 2019; 45 (2): 1803–1811. doi: 10.1016/j.ceramint.2018.10.067
9. Wu Q, Li M, Huang Z, Shao Y, Bai L et al. Well-defined nanostructured core-shell magnetic surface imprinted polymers ( $\text{Fe}_3\text{O}_4@\text{SiO}_2@\text{MIPs}$ ) for effective extraction of trace tetrabromobisphenol A from water. *Journal of Industrial and Engineering Chemistry* 2018; 60: 268–278. doi: 10.1016/j.jiec.2017.11.013
10. Rajkumar S, Prabakaran M. Multi-functional core-shell  $\text{Fe}_3\text{O}_4@\text{Au}$  nanoparticles for cancer diagnosis and therapy. *Colloids and Surfaces B: Biointerfaces* 2019; 174: 252–259. doi: 10.1016/j.colsurfb.2018.11.004
11. Esmailpour M, Sardarian AR, Firouzabadi H. Dendrimer-encapsulated Cu(II) nanoparticles immobilized on superparamagnetic  $\text{Fe}_3\text{O}_4@\text{SiO}_2$  nanoparticles as a novel recyclable catalyst for *N*-arylation of nitrogen heterocycles and green synthesis of 5-substituted 1H-tetrazoles. *Applied Organometallic Chemistry* 2018; 32 (4): e4300–e4316. doi: 10.1002/aoc.4300
12. Ghasemzadeh MA. Synthesis and characterization of  $\text{Fe}_3\text{O}_4@\text{SiO}_2$  NPs as an effective catalyst for the synthesis of tetrahydrobenzo[a]xanthen-11-ones. *Acta Chimica Slovenica* 2015; 62 (4): 977–985. doi: 10.17344/acsi.2015.1501
13. Shiri M, Zolfigol MA, Kruger HG, Tanbakouchian Z. Bis- and trisindolylmethanes (BIMs and TIMs). *Chemical Reviews* 2010; 110 (4): 2250–2293. doi: 10.1021/cr900195a
14. Sujatha K, Perumal PT, Muralidharan D, Rajendran M. Synthesis and anti-microbial activity of pyrazolylbisindoles promising anti-fungal compounds. *Indian Journal of Chemistry* 2009; 48B (2): 267–272. <http://hdl.handle.net/123456789/3432>



15. Pratim Kaishap P, Dohutia C, Chetia D. Synthesis and study of analgesic, anti-inflammatory activities of bis(indolyl) methanes (BIMs). *International Journal of Pharmaceutical Sciences and Research* 2012; 3 (11): 4247–4253. doi: 10.13040/IJPSR.0975-8232.3(11).4247-53
16. Inamoto T, Papineni S, Chintharlapalli S, Cho SD, Safe S et al. 1,1-Bis(3'-indolyl)-1-(*p*-chlorophenyl)methane activates the orphan nuclear receptor Nurr1 and inhibits bladder cancer growth. *Molecular Cancer Therapeutics* 2008; 7 (12): 3825–3833. doi: 10.1158/1535-7163.MCT-08-0730
17. Lee CH, Yao CF, Huang SM, Ko S, Tan YH et al. Novel 2-step synthetic indole compound 1,1,3-tri(3-indolyl)cyclohexane inhibits cancer cell growth in lung cancer cells and xenograft models. *Cancer* 2008; 113 (4): 815–825. doi: 10.1002/cncr.23619
18. Bedekovic D, Fletcher IJ. Recording material containing chromogenic 3,3-bisindolyl-4-azaphthalides. US patent 4,705,776, 1987.
19. Gresens E, Ni Y, Adriaens P, Verbruggen A, Marchal G. Room temperature stable competent cells. US patent 0053911A1, 2004.
20. Babu G, Sridhar N, Perumal PT. A convenient method of synthesis of bis-indolylmethanes: indium trichloride catalyzed reactions of indole with aldehydes and Schiff's bases. *Synthetic Communications* 2000; 30 (9): 1609–1614. doi: 10.1080/00397910008087197
21. Yadav JS, Subba Reddy BV, Basu V, Murthy ChVSR, Mahesh Kumar G et al. Lithium perchlorate catalyzed reactions of indoles: an expeditious synthesis of bis(indolyl)methanes. *Synthesis* 2001; 5: 783–787. doi: 10.1055/s-2001-12777
22. Ji SJ, Wang SY, Zhang Y, Loh TP. Facile synthesis of bis(indolyl)methanes using catalytic amount of iodine at room temperature under solvent-free conditions. *Tetrahedron* 2004; 60 (9): 2051–2055. doi: 10.1016/j.tet.2003.12.060
23. Li-Tao A, Fei-Qing D, Jian-Ping Z, Xiao-Hua L, Li-Li Z. An efficient and solvent-free reaction for synthesis of bis(indol-3-yl)methanes catalyzed by sulfamic acid. *Chinese Journal of Chemistry* 2007; 25 (6): 822–827. doi: 10.1002/cjoc.200790151
24. Bandgar BP, Patil AV, Kamble VT. Fluoroboric acid adsorbed on silica gel catalyzed synthesis of bisindolyl alkanes under mild and solvent-free conditions. *Arkivoc* 2007; xvi: 252–259. doi: 10.3998/ark.5550190.0008.g25
25. Sheng SR, Wang QY, Ding Y, Liu XL, Cai MZ. Synthesis of bis(indolyl)methanes using recyclable PEG-supported sulfonic acid as catalyst. *Catalysis Letters* 2009; 128: 418–422. doi: 10.1007/s10562-008-9767-z
26. Parvanak Boroujeni K, Asadi F, Kazemi R, Fadavi A. Carbon nanotubes grafted with sulfonated polyacrylamide as a heterogeneous catalyst for the preparation of bis(indolyl)methanes. *Journal of Nanoparticle Research* 2019; 21: 151–163. doi: 10.1007/s11051-019-4543-0
27. Parvanak Boroujeni K, Parvanak K. Efficient and solvent-free synthesis of bis-indolylmethanes using silica gel supported aluminium chloride as a reusable catalyst. *Chinese Chemical Letter* 2011; 22 (8): 939–942. doi: 10.1016/j.ccl.2011.01.039
28. Kidwai M, Chauhan R, Bhatnagar D. Nafion-H<sup>+</sup> catalyzed efficient condensation of indoles with aromatic aldehydes in PEG-water solvent system: a green approach. *Arabian Journal of Chemistry* 2016; 9: S2004–S2010. doi: 10.1016/j.arabj.2014.05.009
29. Tong J, Yang CH, Xu DZ. Ionic liquid [DABCO-H][HSO<sub>4</sub>] as a highly efficient and recyclable catalyst for Friedel-Crafts alkylation in the synthesis of bis(naphthol)methane and bis(indolyl)methane derivatives. *Synthesis* 2016; 48 (20): 3559–3566. doi: 10.1055/s-0035-1561655
30. Sobhani S, Jahanshahi R. Nano *n*-propylsulfonated  $\gamma$ -Fe<sub>2</sub>O<sub>3</sub> (NPS- $\gamma$ -Fe<sub>2</sub>O<sub>3</sub>) as a magnetically recyclable heterogeneous catalyst for the efficient synthesis of 2-indolyl-1-nitroalkanes and bis(indolyl)methanes. *New Journal of Chemistry* 2013; 37: 1009–1015. doi: 10.1039/C3NJ40899J
31. Mohapatra SS, Wilson ZE, Roy S, Ley SV. Utilization of flow chemistry in catalysis: new avenues for the selective synthesis of bis(indolyl) methanes. *Tetrahedron* 2017; 73 (14): 1812–1819. doi: 10.1016/j.tet.2017.02.026
32. Tocco G, Zedda G, Casu M, Simbula G, Begala M. Solvent-free addition of indole to aldehydes: unexpected synthesis of novel 1-[1-(1H-indol-3-yl)alkyl]-1H-indoles and preliminary evaluation of their cytotoxicity in hepatocarcinoma cells. *Molecules* 2017; 22 (10): 1747–1757. doi: 10.3390/molecules22101747
33. Wang Y, Sang R, Zheng Y, Guo L, Guan M et al. Graphene oxide: an efficient recyclable solid acid for the synthesis of bis(indolyl)methanes from aldehydes and indoles in water. *Catalysis Communications* 2017; 89: 138–142. doi: 10.1016/j.catcom.2016.09.027
34. Chatterjee R, Mahato S, Santra S, Zyryanov GV, Hajra A et al. Imidazolium Zwitterionic molten salt: an efficient organocatalyst under neat conditions at room temperature for the synthesis of dipyrromethanes as well as bis(indolyl)methanes. *ChemistrySelect* 2018; 3 (14): 5843–5847. doi: 10.1002/slct.201800227
35. Kalla RMN, Hong SC, Kim I. Synthesis of bis(indolyl)methanes using hyper-cross-linked polyaromatic spheres decorated with bromomethyl groups as efficient and recyclable catalysts. *ACS Omega* 2018; 3 (2): 2242–2253. doi: 10.1021/acsomega.7b01925
36. Kasar SB, Thopate SR. Synthesis of bis(indolyl)methanes using naturally occurring, biodegradable itaconic acid as a green and reusable catalyst. *Current Organic Synthesis* 2018; 15 (1): 110–115. doi: 10.2174/1570179414666170621080701
37. Matzkeit YH, Tornquist BL, Manarin F, Botteselle GV, Rafique J et al. Borophosphate glasses: Synthesis, characterization and application as catalyst for bis(indolyl)methanes synthesis under greener conditions. *Journal of Non-Crystalline Solids* 2018; 498: 153–159. doi: 10.1016/j.jnoncrysol.2018.06.020

38. Radfar I, Miraki MK, Ghandi L, Esfandiary N, Abbasi S et al. BF<sub>3</sub>-grafted Fe<sub>3</sub>O<sub>4</sub>@sucrose nanoparticles as a highly efficient acid catalyst for syntheses of dihydroquinazolinones (DHQZs) and bis 3-indolyl methanes (BIMs). *Applied Organometallic Chemistry* 2018; 32 (1): e4431–e4441. doi: 10.1002/aoc.4431
39. Tohidian Z, Hashemi S, Parvanak Boroujeni K. Facile microwave-assisted synthesis of NiO nanoparticles and its effect on soybean (glycine max). *IET Nanobiotechnology* 2019; 13 (2): 101–106. doi: 10.1049/iet-nbt.2018.5003
40. Parvanak Boroujeni K, Tohidian Z, Lorigooini Z, Hamidifar Z, Eskandari MM. Co–Sn–Cu oxides/graphene nanocomposites as green catalysts for preparing 1,8-dioxo-octahydroxanthenes and apoptosis-inducing agents in MCF-7 human breast cancer cells. *IET Nanobiotechnology* 2021; 15 (2): 197–211. doi: 10.1049/nbt2.12006
41. Saei Dehkordi SS, Albadi J, Jafari AA, Samimi HA. Catalytic study of the copper-based magnetic nanocatalyst on the aerobic oxidation of alcohols in water. *Research on Chemical Intermediates* 2021; 47: 2527–2538. doi: 10.1007/s11164-021-04422-w
42. Parvanak Boroujeni K, Tohidian Z, Shahsanaei H, Lorigooini Z, Fadavid A. Silver and palladium nanoparticles anchored to the core-shell Fe<sub>3</sub>O<sub>4</sub>@SiO<sub>2</sub>@Al<sub>2</sub>O<sub>3</sub> for catalytic aerobic oxidation of alcohols and apoptotic induction on MCF-7 cells. *Inorganic Chemistry Communications* 2020; 122: 108206. doi: 10.1016/j.inoche.2020.108206
43. Fathirad F, Mostafavi A, Afzali D. Conductive polymeric ionic liquid/Fe<sub>3</sub>O<sub>4</sub> nanocomposite as an efficient catalyst for the voltammetric determination of amlodipine besylate. *Journal of AOAC INTERNATIONAL* 2017; 100 (2): 406–413. doi: 10.5740/jaoacint.16-0216
44. Ebrahimipour SY, Sheikhshoae I, Castro J, Düsek M, Tohidian Z et al. Synthesis, spectral characterization, structural studies, molecular docking and antimicrobial evaluation of new dioxidouranium (VI) complexes incorporating tetradentate N<sub>2</sub>O<sub>2</sub> Schiff base ligands. *RSC Advances* 2015; 5 (115): 95104–95117. doi: 10.1039/C5RA17524K
45. Tohidian Z, Sheikhshoae I, Khaleghi M, Mague JT. A novel copper (II) complex containing a tetradentate Schiff base: synthesis, spectroscopy, crystal structure, DFT study, biological activity and preparation of its nano-sized metal oxide. *Journal of Molecular Structure* 2017; 1134: 706–714. doi: 10.1016/j.molstruc.2017.01.026
46. Farhadi S, Roostaei-Zaniyani Z. Simple and low-temperature synthesis of NiO nanoparticles through solid-state thermal decomposition of the hexa(amine)Ni(II) nitrate, [Ni(NH<sub>3</sub>)<sub>6</sub>](NO<sub>3</sub>)<sub>2</sub> complex. *Polyhedron* 2011; 30: 1244–1249. doi: 10.1016/j.poly.2011.01.028
47. Farhadi S, Amini MM, Mahmoudi F. Phosphotungstic acid supported on aminosilica functionalized perovskite-type LaFeO<sub>3</sub> nanoparticles: a novel recyclable and excellent visible-light photocatalyst. *RSC Advances* 2016; 6 (105): 102984–102996. doi: 10.1039/C6RA24627C
48. Adel AA, Azza E, Abou-Hussein AA. Spectroscopic studies of bimetallic complexes derived from tridentate or tetradentate Schiff bases of some di- and tri-valent transition metals. *Spectrochimica Acta Part A: Molecular and Biomolecular Spectroscopy* 2006; 64 (4): 1010–1024. doi: 10.1016/j.saa.2005.09.010
49. Wang J, Yang J, Li X, Wei B, Wang D et al. Synthesis of Fe<sub>3</sub>O<sub>4</sub>@SiO<sub>2</sub>@ZnO-Ag core-shell microspheres for the repeated photocatalytic degradation of rhodamine B under UV irradiation. *Journal of Molecular Catalysis A: Chemical* 2015; 406: 97–105. doi: 10.1016/j.molcata.2015.05.023
50. Klug HP, Alexander LE. *X-ray Diffraction Procedures*. 2nd ed., New York: Wiley, 1964.
51. Rahdar A, Nanomedicine Research Journal Aliahmad M, Azizi Y, Keikha N, Moudi M et al. CuO-NiO Nano composites: synthesis, characterization, and cytotoxicity evaluation. 2017; 2 (2), 78–86. doi: 10.22034/NMRJ.2017.56956.1057
52. Fernando Back D, Manzonide Oliveira G, Andre Fontana L, Fiorin Ramao B, Roman D et al. One-pot synthesis, structural characterization, UV–Vis and electrochemical analyses of new Schiff base complexes of Fe(III), Ni(II) and Cu(II). *Journal of Molecular Structure* 2015; 1100: 264–271. doi: 10.1016/j.molstruc.2015.07.050
53. Tohidian Z, Sheikhshoae I. Sonochemical, spectroscopic study and antibacterial activity of two uranyl Schiff base complexes in nano scale. *Rendiconti Lincei* 2017; 28: 405–413. doi: 10.1007/s12210-017-0608-0
54. Gupta D, Meher SR, Illyaskutty N, Alex ZC. Facile synthesis of Cu<sub>2</sub>O and CuO nanoparticles and study of their structural, optical and electronic properties. *Journal of Alloys and Compounds* 2018; 743: 737–745. doi: 10.1016/j.jallcom.2018.01.181
55. Kiziltaş H, Tekin T, Tekin D. Synthesis, characterization of Fe<sub>3</sub>O<sub>4</sub>@SiO<sub>2</sub>@ZnO composite with a core-shell structure and evaluation of its photocatalytic activity. *Journal of Environmental Chemical Engineering* 2020; 8 (5): 104160. doi: 10.1016/j.jece.2020.104160
56. Chen Y, Zhang L, Zhang H, Zhong K, Zhao G et al. Band gap manipulation and physical properties of preferred orientation CuO thin films with nano wheatear array. *Ceramics International* 2018; 44 (1): 1134–1141. doi: 10.1016/j.ceramint.2017.10.070
57. Talluri B, Prasa E, Thomas T. Ultra-small (r<2 nm), stable (>1 year) copper oxide quantum dots with wide band gap. *Superlattices and Microstructures* 2018; 113: 600–607. doi: 10.1016/j.spmi.2017.11.044
58. Banat F, Al-Asheh S, Al-Rawashdeh M. Photodegradation of methylene blue dye by the UV/H<sub>2</sub>O<sub>2</sub> and UV/acetone oxidation processes. *Desalination* 2005; 181 (1–3): 228–232. doi: 10.1016/j.desal.2005.04.005
59. Xia Sh, Zhang L, Pan G, Qian P, Ni Z. Photocatalytic degradation of methylene blue with a nanocomposite system: synthesis, photocatalysis and degradation pathways. *Physical Chemistry Chemical Physics* 2015; 17 (7): 5345–5351. doi: 10.1039/C4CP03877K

60. Kumar B, Smita K, Cumbal L, Debut A, Galeas S, Guerrero VH et al. Phytosynthesis and photocatalytic activity of magnetite ( $\text{Fe}_3\text{O}_4$ ) nanoparticles using the Andean blackberry leaf. *Materials Chemistry and Physics* 2016; 179: 310–315. doi: 10.1016/j.matchemphys.2016.05.045
61. Gnanasekaran L, Hemamalini R, Saravanan R, Ravichandran K, Gracia F et al. Synthesis and characterization of metal oxides ( $\text{CeO}_2$ ,  $\text{CuO}$ ,  $\text{NiO}$ ,  $\text{Mn}_3\text{O}_4$ ,  $\text{SnO}_2$  and  $\text{ZnO}$ ) nanoparticles as photo catalysts for degradation of textile dyes. *Journal of Photochemistry and Photobiology B: Biology* 2017; 173: 43–49. doi: 10.1016/j.jphotobiol.2017.05.027
62. Ding J, Liu L, Xue J, Zhou Z, He G et al. Low-temperature preparation of magnetically separable  $\text{Fe}_3\text{O}_4$ @ $\text{CuO}$ -RGO core-shell heterojunctions for high-performance removal of organic dye under visible light. *Journal of Alloys and Compounds* 2016; 688: 649–656. doi: 10.1016/j.jallcom.2016.07.001
63. Sheikshoaei I, Ramezanpour S, Khatamian M. Synthesis and characterization of thallium doped  $\text{Mn}_3\text{O}_4$  as superior sunlight photocatalysts. *Journal of Molecular Liquids* 2017; 238: 248–253. doi: 10.1016/j.molliq.2017.04.088
64. Dom R, Subasri R, Radha K, Borse PH. Synthesis of solar active nanocrystalline ferrite,  $\text{MFe}_2\text{O}_4$  (M: Ca, Zn, Mg) photocatalyst by microwave irradiation. *Solid State Communications* 2011; 151 (6): 470–473. doi: 10.1016/j.ssc.2010.12.034
65. Nirumand L, Farhadi S, Zabardasti A, Khataee A. Synthesis and sonocatalytic performance of a ternary magnetic MIL-101(Cr)/RGO/ $\text{ZnFe}_2\text{O}_4$  nanocomposite for degradation of dye pollutants. *Ultrasonics Sonochemistry* 2018; 42: 647–658. doi: 10.1016/j.ultsonch.2017.12.033
66. Huang S, Gu L, Zhu N, Feng K, Yuan H et al. Heavy metal recovery from electroplating wastewater by synthesis of mixed- $\text{Fe}_3\text{O}_4$ @ $\text{SiO}_2$ /metal oxide magnetite photocatalysts. *Green Chemistry* 2014; 16 (5): 2696–2705. doi: 10.1039/C3GC42496K